PAPER

Check for updates

Molybdenum-modified ZnIn$_2$S$_4$ with a bifunctional cocatalyst for efficient photocatalytic overall water splitting under simulated sunlight†

Yutong Chen,[a,b] Rong Wu, ✝ *[a,b] Guoan Lin,[d,e] Jianyong Yue,[a,b] Dezheng Kong,[a,b] Chen Zhang,[a,b,c] Shunhang Wei*[c] and Xiaoxiang Xu ✝ *[d,e]

Photocatalytic overall water splitting (POWS) is a promising technique for sustainable hydrogen production that can potentially tackle the current energy and environmental challenges. As a visible-light-active photocatalyst, ZnIn$_2$S$_4$ is an ideal candidate for POWS; however, it exhibits low efficiency due to poor charge separation and improper surface reactions. Here, ZnIn$_2$S$_4$ was modified by doping Mo and depositing a bifunctional cocatalyst for efficient POWS under sunlight. Charge separation and photodeposition of Pt and CrO$_x$ were accelerated by Mo introduction to promote surface POWS reactions and suppress reverse reactions. Under simulated sunlight irradiation, the modified ZnIn$_2$S$_4$ achieved POWS with an apparent quantum efficiency (AQE) of 0.17% at 420 ± 20 nm and a solar-to-hydrogen (STH) conversion efficiency of 0.016%. Theoretical calculations indicated that Mo dopants introduced spin-polarized states at both the conduction band bottom and the valence band top, which are spin-forbidden for charge recombination. This study served as a useful guideline for the design and development of efficient photocatalysts for sunlight-driven POWS.

1. Introduction

Developing hydrogen energy, particularly through sustainable routes, is essential to tackle the challenges of increasing energy needs and environmental degradation.[1] This is typically exemplified by photocatalytic overall water splitting (POWS) using solar energy where hydrogen and oxygen can be produced at the surface of a particulate photocatalyst. Previous studies on POWS have predominantly focused on wide-bandgap semiconductors whose light absorption is limited to UV-light.[2–6] The solar-to-hydrogen (STH) conversion efficiency thereby has intrinsic limitations (<5%) due to their inadequate utilization of solar energy. Developing narrow-bandgap semi-

conductors with visible light absorption is essential to achieve efficient POWS using solar energy.[7]

In this context, transition metal sulfides have garnered significant attention due to their simple structure and ability to absorb visible light photons.[8–11] Among them, ZnIn$_2$S$_4$ is widely studied because of its promising photoelectric properties and catalytic performance.[12–16] However, the rapid recombination of photogenerated electrons and holes in ZnIn$_2$S$_4$ poses a great challenge for POWS.[17,18] Moreover, the surface of ZnIn$_2$S$_4$ is usually deficient in active reaction sites for redox reactions and is subject to photocorrosion due to the vulnerability of the S-terminated surface during water splitting, which is another factor that inhibits POWS reactions.[19–21] Besides, the POWS activity hinges on the proper construction of both reduction and oxidation sites, which would otherwise induce reverse reactions for the product gases H$_2$ and O$_2$.[22,23] Rational cocatalyst deposition is indispensable for POWS not only for the rapid collection of electrons and holes but also for the inhibition of the reverse reaction as well as photocorrosion.[24–28]

In this work, Mo has been uniformly doped into ZnIn$_2$S$_4$, *i.e.* ZnIn$_2$S$_4$:Mo, using a simple one-step hydrothermal method. Mo doping significantly enhances the capture efficiency of photogenerated holes, thereby facilitating charge separation. Meanwhile, Pt and CrO$_x$ cocatalysts with a core–shell structure have been deposited onto ZnIn$_2$S$_4$:Mo, which substantially increases the surface charge transfer efficiency and inhibits reverse reactions. Under optimal conditions, the

[a]Xinjiang Key Laboratory of Solid State Physics and Devices, Xinjiang University, Urumqi, Xinjiang 830017, People's Republic of China
[b]School of Physics Science and Technology, Xinjiang University, Urumqi, Xinjiang 830017, People's Republic of China. E-mail: wurongxju@sina.com
[c]Zhejiang Engineering Research Center of MEMS, Shaoxing University, Shaoxing 312000, China. E-mail: wsh@usx.edu.cn
[d]Clinical and Central Lab, Putuo People's Hospital, Tongji University, Shanghai, 200060, China
[e]School of Chemical Science and Engineering, Tongji University, Shanghai, 200092, China. E-mail: xxxu@tongji.edu.cn
†Electronic supplementary information (ESI) available: XRD, XPS, BET, TEM-EDX, photocatalytic water splitting performance, element content, comparisons of photocatalytic performance and fitting data of TRPL. See DOI: https://doi.org/10.1039/d5dt00316d

photocatalyst exhibits H_2- and O_2-evolution rates of 122.8 μmol g^{-1} h^{-1} and 65.9 μmol g^{-1} h^{-1} under simulated sunlight, respectively.

2. Experimental section

2.1. Chemicals

Zinc acetate dihydrate ($C_4H_6O_4Zn \cdot 2H_2O$, Aladdin, A.R.), indium(III) chloride tetrahydrate ($InCl_3 \cdot 4H_2O$, Macklin, A.R.), thioacetamide (CH_3CSNH_2, Aladdin, A.R.), citric acid ($C_6H_8O_7$, Aladdin, A.R., ≥99.5%(T)), sodium molybdate dihydrate ($Na_2MoO_4 \cdot 2H_2O$, Aladdin; A.R., 99.0%), chromium(III)nitrate nonahydrate ($Cr(NO_3)_3 \cdot 9H_2O$, Aladdin, A.R., 99.0%), and chloroplatinic acid hexahydrate ($H_2PtCl_6 \cdot 6H_2O$, Aladdin, A.R., Pt ≥ 37.5%) were used. All chemicals were used as received without further purification, and deionized water was employed throughout the entire experimental procedure.

2.2 Sample preparation

2.2.1. Synthesis of $ZnIn_2S_4$.
$ZnIn_2S_4$ was prepared through hydrothermal reactions according to the literature.[29] Typically, 2 mmol of zinc acetate dihydrate, 4 mmol of indium(III) chloride tetrahydrate, 10 mmol of thioacetamide, and 1 g of citric acid were dissolved in 60 mL of deionized water with stirring for 30 min. The solution was transferred into a Teflon-lined autoclave (100 mL) and maintained at 180 °C for 24 h. After cooling to room temperature naturally, the obtained product was collected by centrifugation, washed with deionized water and absolute ethanol, and then dried at 80 °C for further characterization.

2.2.2. Synthesis of Mo doped $ZnIn_2S_4$ ($ZnIn_2S_4$:Mo).
To prepare Mo-doped $ZnIn_2S_4$, sodium molybdate dihydrate was added to the reaction solution for hydrothermal synthesis at molar contents of 1%, 3%, and 5%. The reaction conditions were kept the same as those for the synthesis of $ZnIn_2S_4$. The products were denoted as $ZnIn_2S_4$:Mo(x) (x = 1, 3 and 5), where x represents the molar percent of Mo doped into $ZnIn_2S_4$.

2.2.3. Depositing cocatalysts onto $ZnIn_2S_4$:Mo (Pt/CrO_x@$ZnIn_2S_4$:Mo).
The deposition of Pt and CrO_x onto $ZnIn_2S_4$:Mo was carried out *via* photo-reduction of H_2PtCl_6 and photooxidation of $Cr(NO_3)_3$ simultaneously over $ZnIn_2S_4$:Mo. Taking $ZnIn_2S_4$:Mo(3) as an example, 100 mg of $ZnIn_2S_4$:Mo was suspended in an aqueous solution containing appropriate amounts of H_2PtCl_6 and $Cr(NO_3)_3$. The resultant suspensions were irradiated with a 300 W Xe lamp for 1 h. The resultant products were filtered, washed with deionized water and absolute ethanol and dried in a vacuum oven at 60 °C. The resulting catalyst exhibited a deep yellow color and was designated as Pt/CrO_x@$ZnIn_2S_4$:Mo(3) (Scheme 1).

2.3. Catalyst characterization

The microstructure of the sample was examined by field emission scanning electron microscopy (FESEM, Hitachi SU8010, Japan) and transmission electron microscopy (TEM, JEOL JEM-F200, Japan). X-ray diffraction (XRD) patterns were
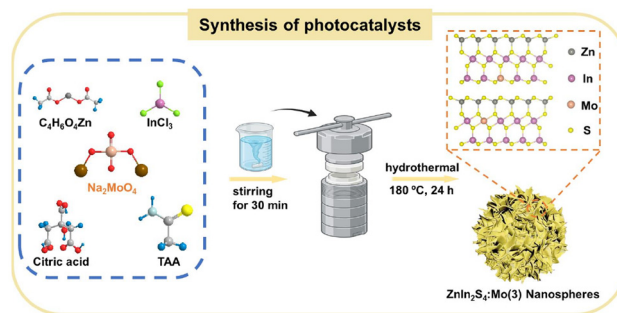
Scheme 1 The schematic representation of $ZnIn_2S_4$:Mo(3) nanospheres.

recorded on an X-ray diffraction instrument (Bruker D8 Advanced, Germany) operating at 60 kV and 50 mA with Cu-Kα radiation. The surface state was investigated utilizing the X-ray photoelectron spectroscopy (XPS) technique with the Thermo Fisher Scientific ESCALAB 250Xi model. The nitrogen adsorption and desorption isotherms at 77 K were obtained using a nitrogen adsorption analyser (Micromeritics ASAP 2460, USA). Prior to measurement, all samples were outgassed under a vacuum at 120 °C for a minimum of 5 hours. UV-vis diffuse reflection spectra (DRS) were obtained using a UV-vis spectrophotometer (Shimadzu UV-3600 plus, Japan) equipped with an integrating sphere assembly. The photoluminescence (PL) spectra were recorded at room temperature with a fluorescence spectrophotometer (Edinburgh FLS1000) using 375 nm as the excitation wavelength. Decay curves were obtained using an FLS980 fluorescence spectrophotometer (Edinburgh Instruments, UK) under the excitation wavelength at 325 nm. The average lifetime (Ave. τ) was calculated according to $\tau = (A_1 \cdot \tau_1^2 + A_2 \cdot \tau_2^2)/(A_1 \cdot \tau_1 + A_2 \cdot \tau_2)$ (τ_i is the lifetime; A_i is the relative intensity). A Bruker EMXplus-6/1 (Germany) was used for the characterization of electron paramagnetic resonance (EPR) with a 300 W Xenon lamp at room temperature. The steady-state surface photovoltage (SPV) spectra were collected using a CEL-SPS1000 spectroscopic analysis system containing a 500 W Xenon lamp (CEL-S500).

2.4. Electrochemical measurements

The experiment was conducted using a CHI760E electrochemical workstation. The experimental setup consisted of a three-electrode cell, with a calomel electrode as the reference electrode, platinum foil as the counter electrode, and a conductive glass electrode coated with a photocatalyst as the working electrode. The electrolyte used was a 0.5 mol L^{-1} Na_2SO_4 solution. For the photoanode preparation, 24 mg of the photocatalyst, 3 mg of acetylene black, and 3 mg of polyvinylidene difluoride were mixed uniformly. Afterwards, an appropriate amount of *N*-methyl pyrrolidone was added through droplet-wise addition. Finally, the resultant suspensions were deposited onto conductive glass and dried at room temperature. Transient photocurrent response measurements were conducted using a 300 W xenon lamp coupled with an

AM1.5G filter as the light source. Electrochemical impedance spectroscopy analysis was performed in the frequency range of 1 to 10^6 Hz. Mott–Schottky measurements were carried out at a frequency of 2000 Hz.

2.5. Computational details

The theoretical calculations of the band structures for $ZnIn_2S_4$ and $ZnIn_2S_4$:Mo(3) were performed using density functional theory (DFT) with a commercial Vienna *ab initio* simulation package. The calculations were performed using the generalized gradient approximation (GGA), Perdew–Burke–Ernzerhof (PBE) function, and projector augmented-wave pseudopotential. A $2 \times 2 \times 2$ cubic unit cell ($a = b = c = 8.26$ Å, $\alpha = \beta = \gamma = 90°$) was used as the structural model. The structures were fully relaxed following the criteria that the forces on each atom are less than 0.02 eV Å^{-1}. An energy cutoff of 400 eV and a total energy of less than 10^{-5} eV were used for static electric potential calculations and geometry optimization, respectively. A Monkhorst–Pack k-points mesh of $5 \times 5 \times 5$ was sampled for all structures.

2.6. Photocatalytic overall water splitting measurement

Photocatalytic tests were performed on a commercial photocatalytic analysis system (Labsolar-6A, Beijing Perfectlight) at ambient temperature. Typically, 50 mg of photocatalysts was dispersed in 100 mL of deionized water (pH = 7). Air in the reaction equipment and solution was vacuumed first. Subsequently, the reactor was exposed to a 300 W Xenon lamp source with an AM1.5G filter. Gas evolution was monitored by on-line gas chromatography (GC9790II, FULI). The stability test was performed under the same conditions over consecutive testing cycles (5 h). The reaction equipment and solution were vacuumed before each testing cycle. The apparent quantum efficiency (AQE) was evaluated using the same system under illumination with different bandpass filters. AQE was calculated according to the following equation:

$$AQY = \frac{2 \times \text{the number of evolved } H_2 \text{ molecules}}{\text{the number of incident photons}} \times 100\%$$

To obtain the STH efficiency, 100 mg of photocatalyst and a 300 W xenon lamp with an AM1.5G filter (100 mW cm^{-2}) were used.

$$STH = \frac{H_2 \text{ production rate (mol s}^{-1}) \times 237 \text{ kJ mol}^{-1}}{\text{energy flux of the incident sunlight (W m}^{-2}) \times \text{irradiation area (m}^{-2})}$$

3. Results and discussion

3.1. Microstructure characterization

The $ZnIn_2S_4$ and $ZnIn_2S_4$:Mo(x) samples were synthesized *via* a one-step hydrothermal method and were characterized by various analytical techniques. Taking $ZnIn_2S_4$:Mo(3) as an example, both pristine $ZnIn_2S_4$ (Fig. 1a and b) and $ZnIn_2S_4$:Mo (3) (Fig. 1c and d) exhibit hierarchical flower-like microstruc-

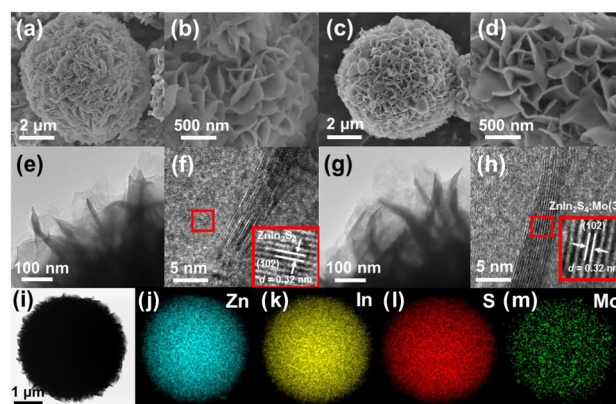**Fig. 1** Scanning electron microscopy images of (a and b) $ZnIn_2S_4$ and (c and d) $ZnIn_2S_4$:Mo(3); transmission electron microscopy and high-resolution transmission electron microscopy images of $ZnIn_2S_4$ (e and f) and $ZnIn_2S_4$:Mo(3) (g and h); (i–m) elemental mapping images of $ZnIn_2S_4$:Mo(3).

tures comprising nanosheets, being consistent with $ZnIn_2S_4$ samples synthesized *via* a hydrothermal method.[30] Mo doping, therefore, can preserve the flower-like microstructures of $ZnIn_2S_4$. To further elucidate the microstructural characteristics, the samples were inspected under HRTEM conditions. The ultra-thin two-dimensional nanosheets were similar before and after Mo doping, as depicted in the figure of pristine $ZnIn_2S_4$ (Fig. 1e) and $ZnIn_2S_4$:Mo(3) (Fig. 1g). In the magnified images, a lattice spacing of 0.32 nm is observed, corresponding to the (102) crystal plane of hexagonal $ZnIn_2S_4$. The elemental mapping of $ZnIn_2S_4$:Mo(3) (Fig. 1i) reveals a uniform dispersion of Zn, In, S, and Mo, providing evidence of the homogeneous doping of Mo in $ZnIn_2S_4$. The molar ratio of Zn/In/S in the $ZnIn_2S_4$:Mo(3) nanosheets is determined to be 1 : 1.66 : 4.00, as detailed in Table S1.† This ratio, in comparison with that of the pristine $ZnIn_2S_4$, indicates a significant reduction in In content, suggesting that Mo atoms likely substitute a fraction of the In atoms within the $ZnIn_2S_4$ lattice.

3.2. Structural and surface analysis

The crystal structures of pristine $ZnIn_2S_4$ and $ZnIn_2S_4$:Mo(x) (where x = 1, 3, 5 atom%) were characterized *via* X-ray diffraction (XRD). As depicted in Fig. 2a and Fig. S1,† pristine $ZnIn_2S_4$ and $ZnIn_2S_4$:Mo(x) showed XRD patterns that matched well with the hexagonal $ZnIn_2S_4$ standard pattern (JCPDS:00-065-2023). The characteristic reflections at 21.6°, 27.7°, 47.5°, 52.4°, and 55.6° correspond to the (006), (102), (110), (116), and (022) crystal planes of hexagonal $ZnIn_2S_4$, respectively. The light absorption capacity of Mo-modified samples was then assessed utilizing UV-vis absorption spectroscopy in Fig. 2b. The spectra indicate that the light absorption capacity of $ZnIn_2S_4$ has been significantly enhanced through Mo doping, as indicated by its increased absorption across the UV, visible, and near-infrared regions.

The elemental states and chemical composition of $ZnIn_2S_4$ before and after Mo doping were investigated by XPS. All core-
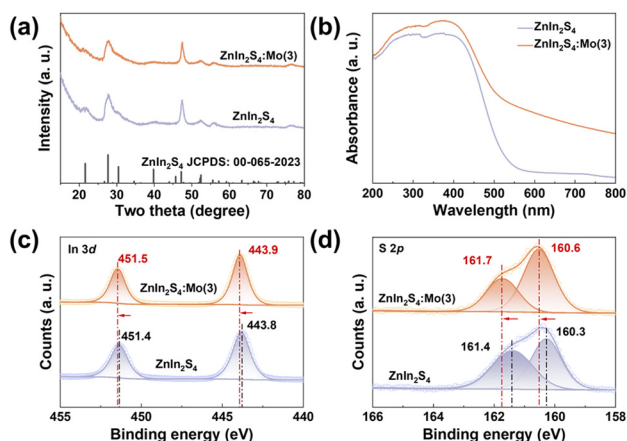
Fig. 2 (a) X-ray diffraction patterns; (b) UV-vis absorption spectra; (c) XPS spectra of In 3d and (d) S 2p of $ZnIn_2S_4$ and $ZnIn_2S_4$:Mo(3).

level binding energies were adjusted with reference to the adventitious C 1s peaks at 284.7 eV. It is noteworthy that the peaks at 443.9 eV and 451.5 eV of $ZnIn_2S_4$:Mo(3) correspond to the In $3d_{5/2}$ and In $3d_{3/2}$ states, exhibiting a slight shift towards higher binding energy compared to $ZnIn_2S_4$ (Fig. 2c). This is probably due to a higher electronegativity of Mo compared to In that tends to attract electrons. Similar results were also observed in the S 2p state, where the peak positions underwent a blue shift of ~0.2 eV (Fig. 2d). The increase can be attributable to the high electronegativity of Mo that results in the electron cloud shift from S towards Mo. The peaks of $ZnIn_2S_4$ and $ZnIn_2S_4$:Mo(3) at 1020.9 eV and 1043.9 eV, respectively, correspond to the Zn $2p_{3/2}$ and Zn $2p_{1/2}$ states (Fig. S2a†). The peaks observed at 228.1 eV and 231.4 eV in $ZnIn_2S_4$:Mo(3) correspond respectively to the Mo $3d_{5/2}$ and Mo $3d_{3/2}$ states, being indicative of Mo^{4+} (Fig. S2b†).[31] Furthermore, Fig. S3a and b† present the N_2 adsorption–desorption isotherms that reveal hysteresis loops for both pristine $ZnIn_2S_4$ and $ZnIn_2S_4$:Mo(3) nanosheets, indicating mesoporous structures (type-IV isotherms). Using the Brunauer–Emmett–Teller (BET) method, we calculated their specific surface area and pore volume. The pristine $ZnIn_2S_4$ nanosheets have a BET specific surface area of 107.2 m^2 g^{-1} and a pore volume of 0.22 cm^3 g^{-1}. In contrast, the $ZnIn_2S_4$:Mo(3) nanosheets have a specific surface area of 117.8 m^2 g^{-1} and a pore volume of 0.23 cm^3 g^{-1}. These results suggest that Mo doping has only trivial impacts on the surface area and pore volume of $ZnIn_2S_4$.

3.3. Photocatalytic performance characterization

The photocatalytic performance of these samples was assessed based on their activity for overall water splitting under simulated AM1.5G conditions. No H_2 and O_2 evolution was detected when using naked $ZnIn_2S_4$ and $ZnIn_2S_4$:Mo(3), implying that the surface of $ZnIn_2S_4$ is unsuitable for POWS reactions. To facilitate water redox reactions, Pt and CrO_x cocatalysts have been deposited onto these samples, which are critical to achieve POWS activity.[32] The successful deposition of these

cocatalysts is confirmed by XPS and TEM analysis (Fig. 4a and b). The Pt 4f spectra are characterized by four overlapping peaks, being attributable to the Pt^0/Pt^{2+} valence state. The surface of $ZnIn_2S_4$ is typically terminated with S anions, which can strongly interact with the metallic Pt cocatalysts by forming Pt–S bonds according to the literature.[33] Similarly, the Cr 3d spectra exhibit two peaks with binding energies of 586.2 eV and 576.1 eV, corresponding to the $2p_{3/2}$ and $2p_{1/2}$ orbitals of Cr^{3+} from CrO_x.[34] The cocatalysts were further inspected by using TEM, HRTEM, and elemental mapping (Fig. 5). The Pt cocatalyst was characterized as small granules with a diameter of approximately 5 nm, while CrO_x appears as an amorphous layer covering the Pt particles. The metallic Pt can be verified by its typical crystal plane spacing of 0.23 nm, corresponding to the Pt (111) crystal plane.[35] Elemental mapping analysis confirms that the deposition of Pt and CrO_x is uniform on the surface of $ZnIn_2S_4$:Mo(3) (Fig. S5c†).

By depositing the Pt and CrO_x cocatalysts, both pristine $ZnIn_2S_4$ and $ZnIn_2S_4$:Mo(3) exhibit POWS activity under simulated sunlight irradiation. The H_2 to O_2 ratio approaches approximately 2 to 1, suggesting successful overall water splitting for these samples.

As illustrated in Fig. 3a, compared with pristine Pt/CrO_x@$ZnIn_2S_4$, a significant enhancement in H_2 and O_2 evolution rates is observed for Pt/CrO_x@$ZnIn_2S_4$:Mo(3), highlighting the importance of Mo doping. The doping content was also optimized to further enhance the POWS activity. As shown in Fig. S4,† doping 3% Mo delivers the highest performance, with H_2 and O_2 evolution rates of 122.8 μmol g^{-1} h^{-1} and 65.9 μmol g^{-1} h^{-1}, respectively. Further increasing the Mo content may lead to the formation of an impurity phase like MoS_2, which serves to block light penetration and impairs the POWS activity (Fig. S5†). $ZnIn_2S_4$ doped with 3% Mo was then used for further stability testing. Fig. 3b demonstrates that Pt/CrO_x@$ZnIn_2S_4$:Mo(3) can stably produce H_2 and O_2 for four consecutive cycles, indicating good stability for POWS reac-
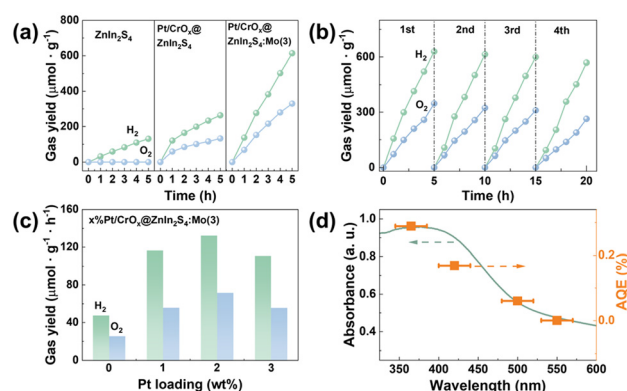

Fig. 3 (a) Comparison of photocatalytic H_2 and O_2 evolution rates for $ZnIn_2S_4$, Pt/CrO_x@$ZnIn_2S_4$, and Pt/CrO_x@$ZnIn_2S_4$:Mo(3); (b) cycling tests of the POWS activity of Pt/CrO_x@$ZnIn_2S_4$:Mo(3); (c) comparison of photocatalytic H_2 and O_2 evolution rates for Pt/CrO_x@$ZnIn_2S_4$:Mo(x) (x = 0, 1, 2, 3); (d) UV-vis light absorption and corresponding wavelength-dependent AQE of Pt/CrO_x@$ZnIn_2S_4$:Mo(3).

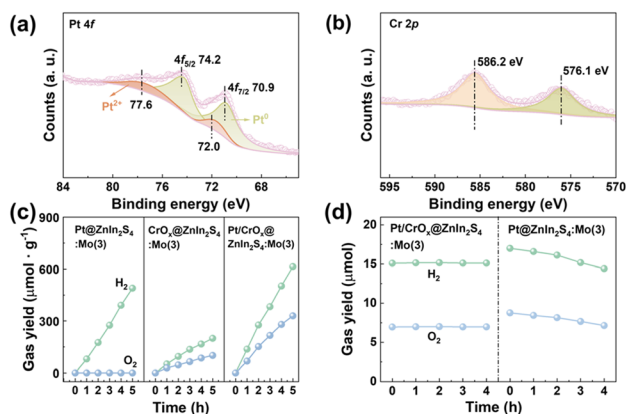**Fig. 4** (a and b) XPS spectra of Pt 4f and Cr 2p for Pt@CrO$_x$/ZnIn$_2$S$_4$:Mo (3); (c) comparison of photocatalytic H$_2$ and O$_2$ evolution rates for Pt@ZnIn$_2$S$_4$:Mo, CrO$_x$@ZnIn$_2$S$_4$:Mo(3) and Pt/CrO$_x$@ZnIn$_2$S$_4$:Mo(3) nanosheets; (d) reverse reaction of Pt/CrO$_x$@ZnIn$_2$S$_4$:Mo(3) and ZnIn$_2$S$_4$: Mo(3).
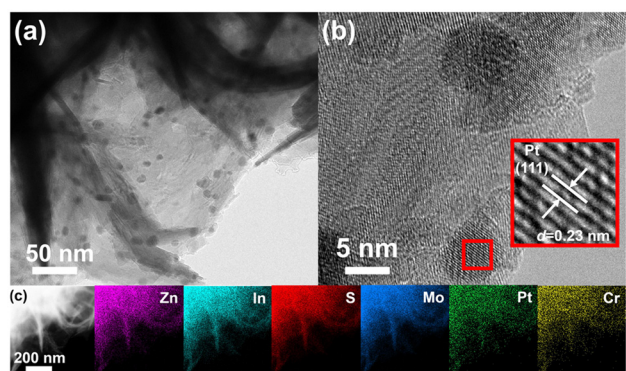

Fig. 5 (a and b) Transmission electron microscopy and elemental mapping images of Pt/CrO$_x$@ZnIn$_2$S$_4$:Mo(3); (c) Transmission electron microscopy and elemental mapping images of Pt/CrO$_x$@ZnIn$_2$S$_4$:Mo(3).

tions. The importance of depositing both Pt and CrO$_x$ can be realized by several control experiments. First, the Pt content was varied from 0% to 3%. The activity of Pt/CrO$_x$@ZnIn$_2$S$_4$: Mo(3) clearly shows an optimal point at 2% (Fig. 3c), suggesting that the presence of Pt modulates the photocatalytic activity. The role of CrO$_x$ can be elucidated through the control experiments with Pt and CrO$_x$ alone. As shown in Fig. 4c, depositing Pt alone on ZnIn$_2$S$_4$:Mo(3) substantially inhibits O$_2$ evolution. This is probably due to the fact that Pt is effective in triggering reverse reactions between H$_2$ and O$_2$ or the oxygen reduction reaction (ORR). This is confirmed by the decrease in H$_2$ and O$_2$ levels in the presence of Pt loaded ZnIn$_2$S$_4$:Mo(3) (Pt@ZnIn$_2$S$_4$:Mo(3), Fig. 4d). This decrease is not observable when Pt is coated with CrO$_x$. Therefore, CrO$_x$ has major contributions to the inhibition of reverse reactions. In addition, depositing CrO$_x$ alone (CrO$_x$@ZnIn$_2$S$_4$:Mo(3)) shows a clear degradation of POWS activity, although the evolution of both H$_2$ and O$_2$ with the correct ratio is observed.

This result indicates that Pt is more effective in promoting POWS reactions than CrO$_x$. Combining these results, it is feasible to rationalize the roles of Pt and CrO$_x$ during POWS reactions. Upon the generation of photo-generated charges in ZnIn$_2$S$_4$:Mo(3) by sunlight, Pt efficiently collects charges for surface redox reactions. The product gases H$_2$ and O$_2$ are isolated from Pt due to the presence of CrO$_x$ which effectively inhibits reverse reactions and/or the ORR. Therefore, there is a collaborative effect between Pt and CrO$_x$ for improving the POWS activity.[36] The POWS activity was further evaluated by collecting the action spectra, as shown in Fig. 3d. It is clear that the photocatalytic activity is photon-driven as the apparent quantum efficiency (AQE) of Pt/CrO$_x$@ZnIn$_2$S$_4$:Mo(3) matches well with the light absorption spectra. The AQE at 420 ± 20 nm reaches 0.17% and the STH is determined to be 0.016%. To the best of our knowledge, these results are competitive with those of ZnIn$_2$S$_4$-based photocatalysts reported for POWS reactions (Table S2†).

3.4. Photoelectrochemical analysis

To clarify the improved POWS activity after Mo doping, we performed photoelectrochemical measurements on ZnIn$_2$S$_4$, ZnIn$_2$S$_4$:Mo(3) and Pt/CrO$_x$@ZnIn$_2$S$_4$:Mo(3). Electrochemical impedance spectroscopy (EIS) spectra are presented in Fig. 6a. The EIS results demonstrate that compared with pristine ZnIn$_2$S$_4$, ZnIn$_2$S$_4$:Mo (3) exhibits a lower charge transfer resistance (R_{ct}), while a further reduced R_{ct} is observed after cocatalyst deposition, indicating that Mo doping and cocatalyst deposition synergistically optimize the water redox reaction conditions. Furthermore, under chopped light irradiation, ZnIn$_2$S$_4$:Mo(3) exhibits a photocurrent density significantly higher than that of ZnIn$_2$S$_4$ yet slightly lower than that of Pt/ CrO$_x$@ZnIn$_2$S$_4$, which aligns well with the photocatalytic performance. These results validate that Mo doping and cocatalyst deposition synergistically accelerate charge separation in ZnIn$_2$S$_4$ (Fig. 6b). This deduction was further confirmed by surface photovoltage (SPV) testing that shows a significant increase in surface photovoltage in ZnIn$_2$S$_4$:Mo(3) and Pt/ CrO$_x$@ZnIn$_2$S$_4$:Mo(3) compared to ZnIn$_2$S$_4$ (Fig. 6c). All these results jointly confirm that the synergistic interaction between Mo doping and the cocatalyst contributes to enhanced charge separation, with the separated charges subsequently migrating to the catalyst surface to drive water redox reactions.

Photoluminescence (PL) is commonly employed to assess the ability of separating and recombining electrons and holes. Fig. 6d shows the photoluminescence spectra of pristine ZnIn$_2$S$_4$, ZnIn$_2$S$_4$:Mo(3), and Pt/CrO$_x$@ZnIn$_2$S$_4$:Mo(3). An emission peak attributable to the band gap transition of ZnIn$_2$S$_4$ nanosheets is evident at 500 nm. The fluorescence intensity of the ZnIn$_2$S$_4$:Mo(3) nanosheets is significantly reduced compared to that of pristine ZnIn$_2$S$_4$. This observation confirms the enhanced separation efficiency of photogenerated electrons and holes by Mo doping. Moreover, Pt/CrO$_x$@ZnIn$_2$S$_4$ shows further reduced PL intensity relative to ZnIn$_2$S$_4$:Mo(3), which highlights that cocatalyst deposition improves photocatalytic activity through additional charge separation pro-
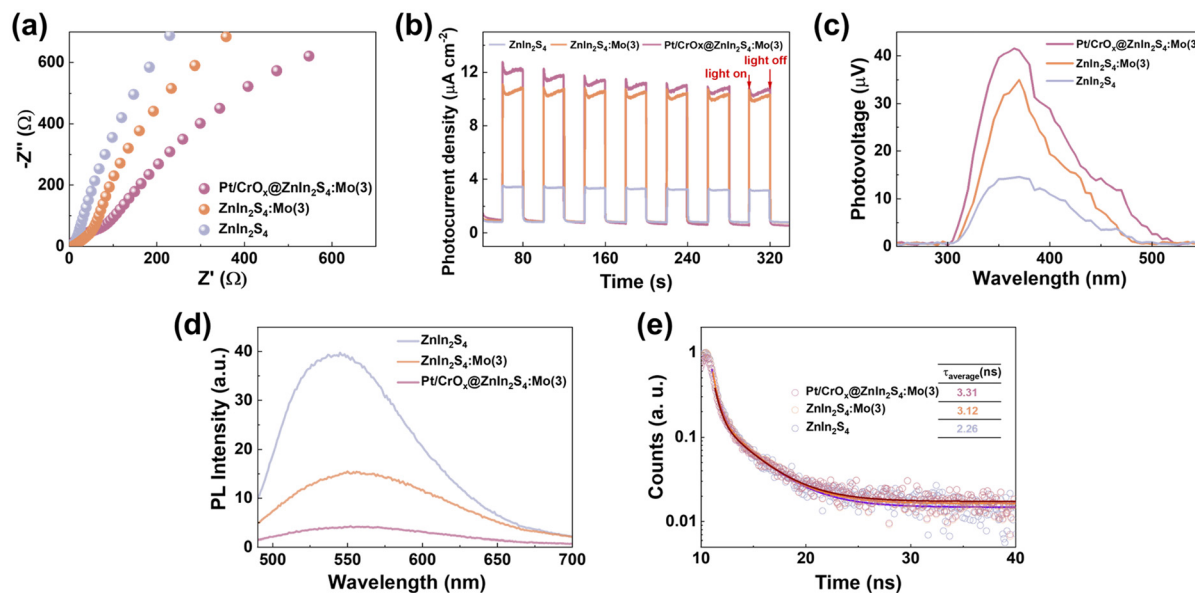
Fig. 6 (a) Electrochemical impedance spectroscopy spectra of $ZnIn_2S_4$, $ZnIn_2S_4$:Mo(3) and Pt/CrO$_x$@$ZnIn_2S_4$:Mo(3); (b) photocurrent measurements of $ZnIn_2S_4$, $ZnIn_2S_4$:Mo(3) and Pt/CrO$_x$@$ZnIn_2S_4$:Mo(3); (c) surface photovoltage of $ZnIn_2S_4$, $ZnIn_2S_4$:Mo(3) and Pt/CrO$_x$@$ZnIn_2S_4$:Mo(3); (d) photo-luminescence spectra of $ZnIn_2S_4$, $ZnIn_2S_4$:Mo(3) and Pt/CrO$_x$@$ZnIn_2S_4$:Mo(3); (e) time-resolved fluorescence spectra of $ZnIn_2S_4$, $ZnIn_2S_4$:Mo(3) and Pt/CrO$_x$@$ZnIn_2S_4$:Mo(3); amplitude-weighted average lifetime is shown in the inset.

motion. The separation dynamics of photoinduced carriers were studied using time-resolved transient photoluminescence (TRPL) decay spectra as shown in Fig. 6e. A two-exponential model was used to fit the TRPL profiles (Table S3†). The prolonged average lifetime (τ) of $ZnIn_2S_4$:Mo(3) compared to pristine $ZnIn_2S_4$ supports more effective electron–hole pair separation in the doped material, while the cocatalyst deposition further enhances charge separation efficiency through optimized carrier migration pathways.

3.5. Theoretical calculations

The impact of Mo doping on the electronic structures of $ZnIn_2S_4$ was investigated using density functional theory (DFT). As depicted in Fig. 7, the band structures, density of states (DOS), and projected density of states (PDOS) of pristine $ZnIn_2S_4$ and $ZnIn_2S_4$:Mo(3) were calculated based on DFT. Both $ZnIn_2S_4$ and $ZnIn_2S_4$:Mo(3) are inherently semiconductors, with calculated bandgaps of 1.136 and 0.671 eV. The band gap values derived from the generalized gradient approximation (GGA) method are known to be underestimated when compared to experimental measurements.[37,38] However, the calculated results can be used for qualitative analysis.[39] It can be seen from the band structure that Mo doping slightly reduces the bandgap of $ZnIn_2S_4$. The bandgap reduction arises from the fact that Mo doping introduces spin-polarized states both at the bottom of the conduction band and at the top of the valence band. These states are mainly contributed by the Mo 4d orbitals that are also strongly hybridized with In 5s and S 3p orbitals according to the PDOS. The behaviour of photo-generated charges, in either the conduction or the valence band, is modulated by these Mo-dominated states that are
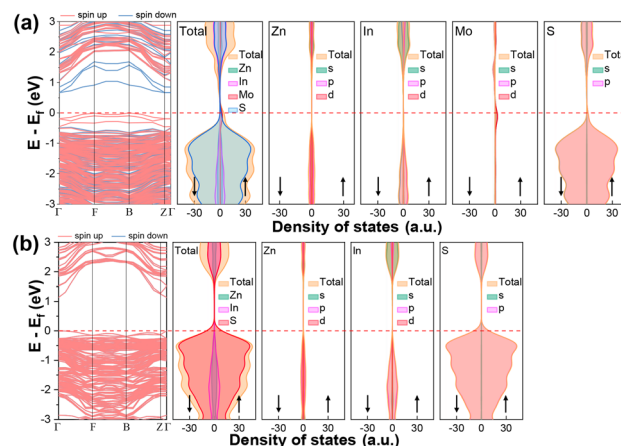

Fig. 7 Band structures, density of states (DOS) and projected density of states (PDOS) for (a) $ZnIn_2S_4$:Mo(3) and (b) $ZnIn_2S_4$. The Fermi level is marked by the dotted lines.

probably the origin of improved charge separation. For instance, the photo-generated electrons and holes could have opposite spins, making their recombination spin-forbidden according to the selection rules, resulting in ameliorated charge separation.

3.6. Band structure analysis

For better understanding the POWS process, the band edge positions of $ZnIn_2S_4$ and $ZnIn_2S_4$:Mo(3) were determined by Mott–Schottky (MS) analysis in conjunction with X-ray photoelectron spectroscopy (XPS) valence band scans. The flat-band

potential (V_{fb}) was calculated based on the Mott–Schottky plot (Fig. 8a) using the following formula:

$$\frac{1}{C^2} = \frac{2}{\varepsilon\varepsilon_0 A^2 e N_D}\left(V - V_{fb} - \frac{k_B T}{e}\right)$$

where C and A are the capacitance at the interface and electrode area, respectively, V is the bias applied, k_B is Boltzmann's constant, N_D is the donor concentration, T is the absolute temperature, ε is the dielectric constant, and e is the electric charge. It can be seen from the MS plot that both samples exhibit positive slopes, indicative of n-type semiconductivity. By examining the intercepts of the MS curves with the energy axis, the flat band potentials of $ZnIn_2S_4$ and $ZnIn_2S_4$:Mo(3) are determined to be 0.50 and 0.36 V vs. RHE, respectively.[40,41] As illustrated in Fig. 8b, the onsets of the valence band of $ZnIn_2S_4$ and $ZnIn_2S_4$:Mo(3) are found to be 1.51 eV and 1.36 eV, respectively. Utilizing the Kubelka–Munk method, the bandgap (E_g) energies were derived from the UV-Vis diffuse reflectance spectra, as depicted in Fig. 8c. The calculated bandgap for $ZnIn_2S_4$:Mo(3) is determined to be approximately 2.40 eV, which is lower than that of $ZnIn_2S_4$ (2.50 eV), being consistent with theoretical calculations. Combining these results, the band edge positions of these two compounds can be deduced, as illustrated in Fig. 8d. $ZnIn_2S_4$:Mo(3) exhibits a slightly reduced band gap and negatively shifted band edge positions compared to $ZnIn_2S_4$ (Fig. 8).

3.7. Photocatalytic mechanism analysis

Based on the above findings and analysis, the mechanism of POWS of Pt/CrO$_x$@ZnIn$_2$S$_4$:Mo(3) under simulated sunlight is illustrated in Scheme 2. Mo doping can effectively modulate the electronic structure of $ZnIn_2S_4$, facilitating charge separation. This improved charge separation is responsible for the high photocatalytic activity. Meanwhile, photodeposition of co-catalysts (Pt and CrO$_x$) plays a vital role during POWS reactions. Pt is mainly responsible for the collection of photo-generated charges and promotes water redox reactions. CrO$_x$
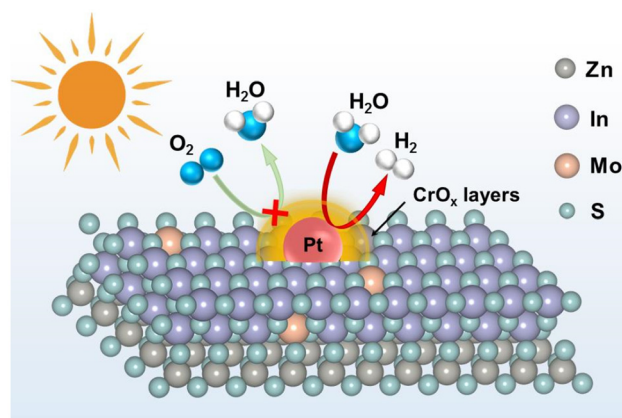
Scheme 2 Mechanism for POWS in the Pt/CrO$_x$@ZnIn$_2$S$_4$:Mo(3) system under simulated sunlight irradiation.

serves as a functional layer that prevents H$_2$ and O$_2$ reverse reactions and the ORR. The synergistic effects between Mo doping, Pt and CrO$_x$ facilitate a smooth POWS reaction at the surface of $ZnIn_2S_4$, with stoichiometric H$_2$- and O$_2$- evolution, under simulated sunlight.

4. Conclusions

In this work, Mo is doped into $ZnIn_2S_4$ using a simple one-step hydrothermal method, followed by photo-deposition of Pt and CrO$_x$ cocatalysts for POWS reactions. The Mo doping introduces spin-polarized states at both the conduction band bottom and the valence band top, which are spin-forbidden for charge recombination and beneficial for charge separation. Depositing Pt facilitates charge collection and surface redox reactions. CrO$_x$ serves as a functional layer covering Pt, which is critical for inhibiting water-splitting reverse reactions and the ORR. Under optimal conditions, the photocatalytic systems achieve average H$_2$- and O$_2$- evolution rates of 122.8 μmol g^{-1} h^{-1} and 65.9 μmol g^{-1} h^{-1}, respectively, under simulated sunlight irradiation. An AQE of 0.17% at 420 ± 20 nm and an STH of 0.016% have been obtained. This study proposes a novel strategy for POWS through the synergistic effect of element doping and co-catalyst deposition, offering a promising guideline for the development of photocatalysts for efficient solar-driven water-splitting reactions.

Author contributions

Yutong Chen: investigation, conceptualization, data curation, methodology, formal analysis, and writing – original draft. Rong Wu: supervision and writing – review & editing. Guoan Lin: theoretical calculations. Jianyong Yue: investigation, methodology, and validation. Dezheng Kong: investigation, methodology, and validation. Chen Zhang: investigation, methodology, and validation. Shunhang Wei: supervision and writing – review & editing. Xiaoxiang Xu: supervision and
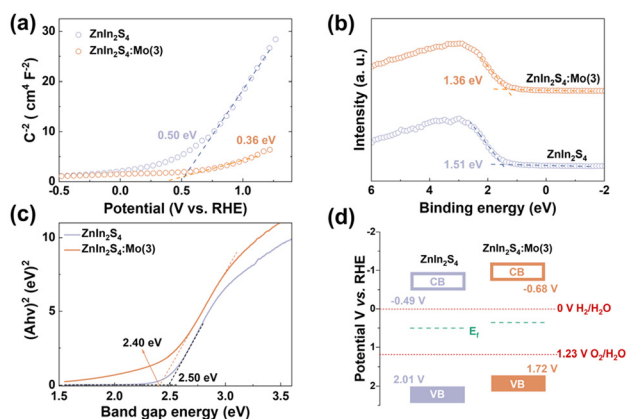

Fig. 8 (a) Mott–Schottky plots of ZnIn$_2$S$_4$ and ZnIn$_2$S$_4$:Mo(3); (b) XPS VB spectra of ZnIn$_2$S$_4$ and ZnIn$_2$S$_4$:Mo(3); (c) Tauc plot of ZnIn$_2$S$_4$ and ZnIn$_2$S$_4$:Mo(3); (d) band structures of ZnIn$_2$S$_4$ and ZnIn$_2$S$_4$:Mo(3).

writing – review & editing. All authors have given approval to the final version of the manuscript.

Data availability

The data supporting this article have been included as part of the ESI.†

Conflicts of interest

There are no conflicts to declare.

Acknowledgements

References

1 S. Chen, T. Takata and K. Domen, Particulate photocatalysts for overall water splitting, *Nat. Rev. Mater.*, 2017, **2**, 17050.

2 W. Lei, Y. Wang, H. Wang, N. Suzuki, C. Terashima and A. Fujishima, Gelation-induced controlled synthesis of TiO_2 with tunable phase transition for efficient photocatalytic hydrogen evolution, *Inorg. Chem. Front.*, 2024, **11**, 2178–2186.

3 C. Li, H. Che, P. Huo, Y. Yan, C. Liu and H. Dong, Confinement of ultrasmall $CoFe_2O_4$ nanoparticles in hierarchical $ZnIn_2S_4$ microspheres with enhanced interfacial charge separation for photocatalytic H_2 evolution, *J. Colloid Interface Sci.*, 2021, **581**, 764–773.

4 X.-J. Lu, I. Ullah, J.-H. Li, S. Chen, C.-Z. Yuan and A.-W. Xu, A bimetallic CoZn metal–organic-framework derived CoZnS@NSC Co-catalyst loaded on g-C_3N_4 for significantly augmented photocatalytic H_2 evolution, *Inorg. Chem. Front.*, 2024, **11**, 3435–3445.

5 F. Xing, J. Li, C. Wang, S. Jin, H. Jin and J. Li, Efficient photocatalytic hydrogen evolution of g-C_3N_4/Vs-SnS_2/CdS through a sulfur vacancy-rich SnS_2 induced charge storage effect, *Inorg. Chem. Front.*, 2024, **11**, 2884–2893.

6 S. Zhang, X. Liu, C. Liu, S. Luo, L. Wang, T. Cai, Y. Zeng, J. Yuan, W. Dong, Y. Pei and Y. Liu, MoS_2 Quantum Dot Growth Induced by S Vacancies in a $ZnIn_2S_4$ Monolayer: Atomic-Level Heterostructure for Photocatalytic Hydrogen Production, *ACS Nano*, 2018, **12**, 751–758.

7 X. Liu, L. Yan, W. Li, K. Chen, F. Wang, J. Xiao, T. Hisatomi, T. Takata and K. Domen, Enhancing the Photocatalytic Activity of $CaTaO_2N$ for Overall Water Splitting through Surface Nitride Ion Enrichment, *ACS Catal.*, 2024, **14**, 10561–10567.

8 P. Kulkarni, S. K. Nataraj, R. G. Balakrishna, D. H. Nagaraju and M. V. Reddy, Nanostructured binary and ternary metal sulfides: synthesis methods and their application in energy conversion and storage devices, *J. Mater. Chem. A*, 2017, **5**, 22040–22094.

9 Y. Li, H. Dong, L. Li, L. Tang, R. Tian, R. Li, J. Chen, Q. Xie, Z. Jin, J. Xiao, S. Xiao and G. Zeng, Recent advances in waste water treatment through transition metal sulfides-based advanced oxidation processes, *Water Res.*, 2021, **192**, 116850.

10 R. Kalia, B. M. Pirzada, R. K. Kunchala and B. S. Naidu, Noble metal free efficient photocatalytic hydrogen generation by TaON/CdS semiconductor nanocomposites under natural sunlight, *Int. J. Hydrogen Energy*, 2023, **48**, 16246–16258.

11 R. Kalia, P. Yadav, A. Verma, J. Yadav and B. S. Naidu, Natural sunlight induced photocatalytic hydrogen evolution by $SrTaO_2N$/CdS nanocomposites, *J. Alloys Compd.*, 2025, **1015**, 178790.

12 S. Shen, J. Chen, X. Wang, L. Zhao and L. Guo, Microwave-assisted hydrothermal synthesis of transition-metal doped $ZnIn_2S_4$ and its photocatalytic activity for hydrogen evolution under visible light, *J. Power Sources*, 2011, **196**, 10112–10119.

13 R. Yang, L. Mei, Y. Fan, Q. Zhang, R. Zhu, R. Amal, Z. Yin and Z. Zeng, $ZnIn_2S_4$-Based Photocatalysts for Energy and Environmental Applications, *Small Methods*, 2021, **5**, 2100887.

14 T. Zhang, T. Wang, F. Meng, M. Yang and S. Kawi, Recent advances in $ZnIn_2S_4$-based materials towards photocatalytic purification, solar fuel production and organic transformations, *J. Mater. Chem. C*, 2022, **10**, 5400–5424.

15 X. Zheng, Y. Song, Y. Liu, Y. Yang, D. Wu, Y. Yang, S. Feng, J. Li, W. Liu, Y. Shen and X. Tian, $ZnIn_2S_4$-based photocatalysts for photocatalytic hydrogen evolution via water splitting, *Coord. Chem. Rev.*, 2023, **475**, 214898.

16 P. Yadav and B. S. Naidu, in *Green Hydrogen Economy for Environmental Sustainability. Volume 1: Fundamentals and Feedstocks*, American Chemical Society, 2024, ch. 6, vol. 1473, pp. 119–146.

17 W. Guan, L. Zhang, P. Wang, Y. Wang, H. Wang, X. Dong, M. Meng, L. Sui, Z. Gan, L. Dong and L. Yu, Highly Efficient Photocatalytic Hydrogen Evolution over Mo-Doped $ZnIn_2S_4$ with Sulfur Vacancies, *Nanomaterials*, 2022, **12**, 3980.

18 H. Su, C. Rao, L. Zhou, Y. Pang, H. Lou, D. Yang and X. Qiu, Mo-Doped/Ni-supported $ZnIn_2S_4$-wrapped $NiMoO_4$ S-scheme heterojunction photocatalytic reforming of lignin into hydrogen, *Green Chem.*, 2022, **24**, 2027–2035.

19 F. Huang, Z. Li, Y. Xu, A. Yan, T. Zhang, Q. Wang, S. Li, S. Lu, W. Zhao, Y. Gao and J. Zhang, Excellent anti-photocorrosion and hydrogen evolution activity of $ZnIn_2S_4$-based photocatalysts: *In situ* design of photogenerated charge dynamics, *Chem. Eng. J.*, 2023, **473**, 145430.

20 H. Su, H. Lou, Z. Zhao, L. Zhou, Y. Pang, H. Xie, C. Rao, D. Yang and X. Qiu, *In situ* Mo doped $ZnIn_2S_4$ wrapped MoO_3 S-scheme heterojunction via Mo-S bonds to enhance photocatalytic HER, *Chem. Eng. J.*, 2022, **430**, 132770.

21 F. Xing, Q. Liu and C. Huang, Mo-Doped $ZnIn_2S_4$ Flower-Like Hollow Microspheres for Improved Visible Light-Driven Hydrogen Evolution, *Sol. RRL*, 2020, **4**, 1900483.

22 A. S. Alotabi, T. D. Small, Y. Yin, D. J. Osborn, S. Ozaki, Y. Kataoka, Y. Negishi, K. Domen, G. F. Metha and G. G. Andersson, Reduction and Diffusion of Cr-Oxide Layers into P25, $BaLa_4Ti_4O_{15}$, and Al:$SrTiO_3$ Particles upon High-Temperature Annealing, *ACS Appl. Mater. Interfaces*, 2023, **15**, 14990–15003.

23 R. Li, T. Takata, B. Zhang, C. Feng, Q. Wu, C. Cui, Z. Zhang, K. Domen and Y. Li, Criteria for Efficient Photocatalytic Water Splitting Revealed by Studying Carrier Dynamics in a Model Al-doped $SrTiO_3$ Photocatalyst, *Angew. Chem., Int. Ed.*, 2023, **62**, e202313537.

24 K. Chen, J. Xiao, J. J. M. Vequizo, T. Hisatomi, Y. Ma, M. Nakabayashi, T. Takata, A. Yamakata, N. Shibata and K. Domen, Overall Water Splitting by a $SrTaO_2N$-Based Photocatalyst Decorated with an Ir-Promoted Ru-Based Cocatalyst, *J. Am. Chem. Soc.*, 2023, **145**, 3839–3843.

25 L. Lin, P. Kaewdee, V. Nandal, R. Shoji, H. Matsuzaki, K. Seki, M. Nakabayashi, N. Shibata, X. Tao, X. Liang, Y. Ma, T. Hisatomi, T. Takata and K. Domen, Flux-Assisted Synthesis of $Y_2Ti_2O_5S_2$ for Photocatalytic Hydrogen and Oxygen Evolution Reactions, *Angew. Chem., Int. Ed.*, 2023, **62**, e202310607.

26 Y. Qi, B. Zhang, G. Zhang, Z. Zheng, T. Xie, S. Chen, G. Ma, C. Li, K. Domen and F. Zhang, Efficient overall water splitting of a suspended photocatalyst boosted by metal-support interaction, *Joule*, 2024, **8**, 193–203.

27 J. Xiao, M. Nakabayashi, T. Hisatomi, J. J. M. Vequizo, W. Li, K. Chen, X. Tao, A. Yamakata, N. Shibata, T. Takata, Y. Inoue and K. Domen, Sub-50 nm perovskite-type tantalum-based oxynitride single crystals with enhanced photoactivity for water splitting, *Nat. Commun.*, 2023, **14**, 8030.

28 W. Li, W. Duan, G. Liao, F. Gao, Y. Wang, R. Cui, J. Zhao and C. Wang, 0.68% of solar-to-hydrogen efficiency and high photostability of organic-inorganic membrane catalyst, *Nat. Commun.*, 2024, **15**, 6763.

29 H. Jing, G. Xu, B. Yao, J. Ren, Y. Wang, Z. Fang, Q. Liang, R. Wu and S. Wei, Sulfur Vacancy-Enriched Rhombohedral $ZnIn_2S_4$ Nanosheets for Highly Efficient Photocatalytic Overall Water Splitting under Visible Light Irradiation, *ACS Appl. Energy Mater.*, 2022, **5**, 10187–10195.

30 H. Jing, J. Ren, J. Yue, S. Liu, Q. Liang, R. Wu, Y. Wang, Z. Fang, H. Li and S. Wei, $ZnIn_2S_4$ with oxygen atom doping and surface sulfur vacancies for overall water splitting under visible light irradiation, *Catal. Sci. Technol.*, 2023, **13**, 226–232.

31 Y. Liu, Y. Li, F. Peng, Y. Lin, S. Yang, S. Zhang, H. Wang, Y. Cao and H. Yu, 2H- and 1T- mixed phase few-layer MoS_2 as a superior to Pt co-catalyst coated on TiO_2 nanorod arrays for photocatalytic hydrogen evolution, *Appl. Catal., B*, 2019, **241**, 236–245.

32 T. Ma, W. Li, J. Li, W. Duan, F. Gao, G. Liao, J. Li and C. Wang, Multisite Cocatalysis: Single atomic Pt^{2+}/Pt^0 active sites synergistically improve the simulated sunlight driven H_2O-to-H_2 conversion performance of Sb2S3 nanorods, *J. Colloid Interface Sci.*, 2024, **658**, 476–486.

33 R. Wang, L. Shi, E. Y. Konysheva and X. Xu, Selective Photocatalysis of Benzyl Alcohol Valorization by Cocatalyst Engineering Over $Zn_2In_2S_5$ Nanosheets, *Adv. Funct. Mater.*, 2024, 2418074.

34 T. Higashi, K. Seki, Y. Sasaki, Y. Pihosh, V. Nandal, M. Nakabayashi, N. Shibata and K. Domen, Mechanistic Insights into Enhanced Hydrogen Evolution of CrO/Rh Nanoparticles for Photocatalytic Water Splitting, *Chem. – Eur. J.*, 2023, **29**, e202204058.

35 Q. Li, C. Cui, H. Meng and J. Yu, Visible-Light Photocatalytic Hydrogen Production Activity of $ZnIn_2S_4$ Microspheres Using Carbon Quantum Dots and Platinum as Dual Co-catalysts, *Chem. – Asian J.*, 2014, **9**, 1766–1770.

36 T. Takata, J. Jiang, Y. Sakata, M. Nakabayashi, N. Shibata, V. Nandal, K. Seki, T. Hisatomi and K. Domen, Photocatalytic water splitting with a quantum efficiency of almost unity, *Nature*, 2020, **581**, 411–414.

37 B. Neupane, H. Tang, N. K. Nepal, S. Adhikari and A. Ruzsinszky, Opening band gaps of low-dimensional materials at the meta-GGA level of density functional approximations, *Phys. Rev. Mater.*, 2021, **5**, 063803.

38 Y.-N. Zhang, M. Zhang, P. Zhang and W.-B. Hu, Investigation of electronic structure and optoelectronic properties of Si-doped β-Ga_2O_3 using GGA + U method based on first-principle, *Acta Phys. Sin.*, 2024, **73**, 017102-017101–017102-017110.

39 H. Xiao, J. Tahir-Kheli and W. A. Goddard III, Accurate Band Gaps for Semiconductors from Density Functional Theory, *J. Phys. Chem. Lett.*, 2011, **2**, 212–217.

40 G. Lin and X. Xu, Ba-Modified $LaTiO_2N$ as an Efficient Visible Light Active Photocatalyst for Water Oxidation, *ACS Sustainable Chem. Eng.*, 2020, **8**, 9641–9649.

41 Y. Wang, S. Jin, G. Pan, Z. Li, L. Chen, G. Liu and X. Xu, Zr doped mesoporous $LaTaON_2$ for efficient photocatalytic water splitting, *J. Mater. Chem. A*, 2019, **7**, 5702–5711.